SCIENCE CHINA
Information Sciences

• RESEARCH PAPER •

April 2023, Vol. 66 142404:1–142404:7
https://doi.org/10.1007/s11432-022-3549-7

Mid-infrared plasmonic silicon quantum dot/HgCdTe photodetector with ultrahigh specific detectivity

Yueying CUI[1†], Zhouyu TONG[2†], Xinlei ZHANG[1], Wenhui WANG[1], Weiwei ZHAO[1], Yuanfang YU[1*], Xiaodong PI[2], Jialin ZHANG[1] & Zhenhua NI[1*]

[1]*School of Physics and Key Laboratory of MEMS of Ministry of Education, Southeast University, Nanjing* 211189*, China;*
[2]*State Key Laboratory of Silicon Materials, School of Materials Science and Engineering, Zhejiang University, Hangzhou* 310027*, China*

Received 14 April 2022/Revised 4 May 2022/Accepted 8 July 2022/Published online 15 March 2023

Abstract Highly sensitive photodetectors operating at mid-infrared (MIR) wavelengths are urgently required for the applications of astronomy, optical communication, security monitoring, and so forth. However, further promoting the sensitivity in conventional MIR devices for a higher detectivity is challenging. Among the potential strategies, integrating localized surface plasmon resonance with MIR semiconductors is a promising approach to developing high-performance optoelectronics. Here we demonstrate a high-sensitivity boron (B)-doped silicon quantum dot (Si-QD)/HgCdTe (MCT) MIR photodetector. Because of plasmon-induced hot-hole tunneling and enhanced light absorption, the hybrid photodetector exhibits a high specific detectivity of $\sim 1.6\times10^9$ cm·Hz$^{1/2}$·W^{-1} (Jones) and a high-speed response ($\sim$224 ns for the rise time and $\sim$580 ns for the fall time) at room temperature. Furthermore, the device achieves high-performance spectral blackbody detection with a peak detectivity of up to 1.6×10^{11} Jones at $\sim$5.8 μm under a cryogenic environment of 77 K, higher than that of bare MCT. This prominent enhancement can be attributed to the further suppression of hot-hole cooling due to a reduced phonon population at low temperatures, which facilitates more efficient hot-carrier extraction and contributes to ultrahigh sensitivity. The plasmonic material-integrated MCT architecture can pave the way for developing high-performance MIR photodetection.

Keywords doped silicon quantum dots, HgCdTe, localized surface plasmon resonance, hot-hole tunneling, mid-infrared photodetector

Citation Cui Y Y, Tong Z Y, Zhang X L, et al. Mid-infrared plasmonic silicon quantum dot/HgCdTe photodetector with ultrahigh specific detectivity. Sci China Inf Sci, 2023, 66(4): 142404, https://doi.org/10.1007/s11432-022-3549-7

1 Introduction

Photodetectors operating at mid-infrared (MIR) wavelengths play a key role in astronomical work [1], medical diagnosis [2], security monitoring [3], and so on [4–10]. HgCdTe (MCT) [11–13], InSb [14], InGaAs [15], and InAs [16] are primary candidates for MIR applications with mature preparation technology. As a variable bandgap alloy, MCT demonstrates broadband response spectra ranging from 1 to 30 μm [17–19]. However, even in a cryogenic environment, MCT detectivity is still far from the theoretical limit [20]. Filling this gap by pursuing state-of-the-art MIR applications is challenging. In recent years, colloidal quantum dots (CQDs) have been considered excellent candidates for optoelectronic devices because of the strong light-matter interaction, quantum confinement effects, and unique carrier dynamics [21–25]. Among all types of CQDs, Si QDs have attracted widespread attention due to their high stability and compatibility with Si-based technologies [26, 27]. Moreover, the highly modulable localized surface plasmon resonance (LSPR) in the MIR region can be excited in heavily doped Si QDs [28–30]. By confining light into a nanostructure with subwavelength dimensions, LSPR can greatly enhance scattering or absorption at resonance wavelengths [29,31,32]. LSPR in plasmonic, heavily doped

* Corresponding author (email: yfyu@seu.edu.cn, zhni@seu.edu.cn)
† Cui Y Y and Tong Z Y have the same contribution to this work.

Si QDs can decay nonradiatively through Landau damping and generate hot carriers [30]. Hot carriers with adequate excess kinetic energy can tunnel through the interfacial barrier and contribute to a remarkable photoresponse [33, 34]. Hence, the heavily doped QDs with LSPR can be used to promote MCT performance. In this work, a high-performance B-doped Si-QD/MCT photodetector with an ultrahigh specific detectivity and a fast photoresponse is demonstrated. The LSPR of B-doped Si QDs obviously improves the light absorption in the MIR region. Plasmon-induced hot holes in B-doped Si QDs can participate in photoelectric conversion, resulting in an improved specific detectivity of MCT. In a cryogenic environment (77 K), the sensitivity of the plasmonic Si-QD/MCT photodetector reaches $\sim$1.6$\times$10^{11} cm·Hz$^{1/2}$·W^{-1}(Jones) at $\sim$5.8 μm. Hot-hole tunneling is adequately fast to prevail over the defect trapping processes in B-doped Si QDs; therefore, the device maintains a high-speed photoresponse, with a rise time of $\sim$224 ns and a fall time of $\sim$580 ns. These results indicate that combining plasmonic nanostructures with infrared semiconductors is an effective approach for implementing advanced MIR devices.

2 Results and discussion

Colloidal B-doped Si QDs were spin-coated on top of MCT to form a Si-QD/MCT hybrid photodetector, and the schematic diagram is shown in Figure 1(a). The thickness of ZnS is $\sim$10 nm, which acts as an antireflection coating and prevents the oxidation of MCT. Figure 1(b) illustrates the operation mechanisms of the Si-QD/MCT hybrid devices. First, free-carrier oscillation inside the doped Si QDs is excited by the incident light waves, resulting in strong LSPR and improved light absorption in the MIR region. Then, the hot holes generated in the Si QDs can tunnel through the ZnS layer and enter the MCT, and finally be collected using an external circuit. Si QDs with a B-doping concentration of 13.66% are used in this work. A transmission electron microscopy (TEM) image of the Si QDs is shown in Figures 1(c) and (d). The spherical shape in the TEM images (Figure 1(c)) demonstrates the formation of Si QDs in this work. The EDS mapping reveals the presence of Si and B elements (Figure 1(c)), confirming the B doping in Si QDs. The lattice fringes of the Si QDs can be distinctly observed in the high-resolution transmission electron microscopy (HRTEM) images (Figure 1(d)). The concentric stripes in the selected area electron diffraction (SAED) result (inset of Figure 1(d)) present the good crystallinity of the Si QDs. The statistical results in Figure 1(e) show that the average size of the Si QDs is $\sim$5.5 nm. The Fourier transform infrared spectroscopy (FTIR) spectrum of the Si QDs in Figure 1(f) shows that the LSPR peak is located at $\sim$3.75 μm. Notably, the LSPR of the B-doped Si QDs can be further tuned by optimizing the doping level and particle size [29, 35].

Figure 2(a) illustrates the photoresponse characteristics of the B-doped Si-QD/MCT photodetector under different power densities at 4 μm. According to Figure 2(b), when the power density of incident laser gradually changes from 0.16 to 16 mW·cm^{-2}, the photocurrent increases from 0.26 to 9.97 μA. In addition, the photodetector also presents high specific detectivity D^*, calculated by [36, 37]

$$D^* = R\sqrt{\frac{A}{2eI_{\rm dark}}}, \tag{1}$$

$$R = \frac{I_{\rm ph}}{P}, \tag{2}$$

where R is the responsivity, A is the sensitive area of the device channel, e is the electron charge, $I_{\rm dark}$ is the dark current, $I_{\rm ph}$ is the photocurrent, and P is the effective power. The maximum specific detectivity can reach $\sim$1.6$\times$10^9 Jones at 4 μm. In addition, the photocurrent of the hybrid devices can be effectively tuned when applying different bias voltage ($V_{\rm ds}$), as seen in Figure 2(c). Figure 2(d) shows the specific detectivity of the photodetector under different MIR wavelengths at fixed power density of 1.6 mW·cm^{-2}. The device has a peak specific detectivity located between 3.4 and 4.0 μm. The device also presents an ultra-fast photoresponse measured at 2.8 μm. The rise and fall regions of the curve are well fitted by a single exponential function (Supplementary Information) with $\sim$224 ns for the rise time and $\sim$580 ns for the fall time (see Figure 2(e)).

Blackbody response is an essential measurement for the sensitivity of infrared photodetectors to reliably assess their potential for practical applications [38]. The blackbody detectivity of the photodetector under different radiation wavelengths (D^*_λ) is obtained by the combination of photocurrent spectra with

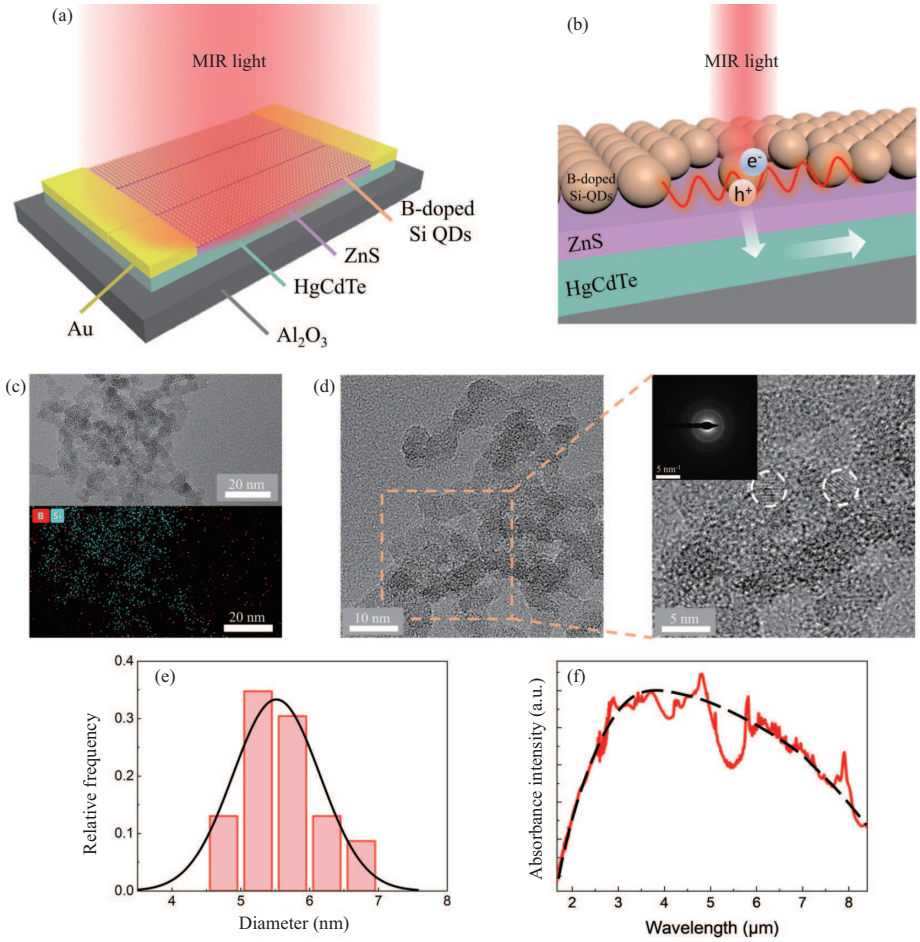

Figure 1 (Color online) (a) Schematic illustration of the B-doped Si-QD/MCT device structure. (b) Schematic of hot-hole generation and tunneling in the device under MIR light irradiation. (c) TEM and EDS images of the B-doped Si QDs. (d) HRTEM images of the B-doped Si QDs, and the inset is the SAED result (scale bar of inset image is 5 nm^{-1}). (e) Diameter distribution of the B-doped Si QDs. Their size in multiple TEM micrographics was factored into a size distribution histogram and fitted using a Gaussian function. (f) Normalized FTIR spectrum of the B-doped Si QDs.

blackbody response result [12, 39, 40].

$$D^* = \frac{R}{V_n}\sqrt{A \cdot \Delta f}, \tag{3}$$

$$D^*_\lambda = \frac{D^* \cdot f(\lambda)_{\mathrm{FTIR}}}{G}, \tag{4}$$

where R is blackbody responsivity, V_n is detector noise voltage, Δf is spectrum analyzer bandwidth, $f(\lambda)_{\mathrm{FTIR}}$ is the normalized FTIR relative response spectrum (Figure C1, Supporting Information), G factor is the ratio of the peak responsivity of the detector to the blackbody responsivity, obtained from the relative response spectrum [12]. Figure 3(a) shows the blackbody detectivity of the pure MCT photodetector and B-doped Si-QD/MCT photodetector under blackbody radiation with a bias current of 1 mA at 300 K. The blackbody detectivity of the B-doped Si-QD/MCT photodetector is slightly improved when the wavelength ranges from ∼3 to ∼4 μm, which is in agreement with the absorption peak of the B-doped Si QDs at 300 K. On the other hand, the blackbody detectivity of the MCT devices at low temperature of 77 K is dramatically enhanced after sensitizing with the B-doped Si QDs, see Figure 3(b). The peak blackbody detectivity of B-doped Si-QD/MCT device reaches ∼1.6×10^{11} Jones at ∼5.8 μm, which is about twice that of pure MCT device. As the temperature drops from 300 to 77 K, the peak blackbody detectivity of MCT devices shifts from ∼4.49 to ∼5.55 μm and the upper spectral response limit shifts from ∼5.34 to ∼6.91 μm, due to the temperature dependent band gap of MCT (Supplementary Information) narrowing from 0.237 to 0.179 eV [41, 42]. In addition, the peak position of enhanced blackbody detectivity in photodetector also shows red-shifts, mainly attributed

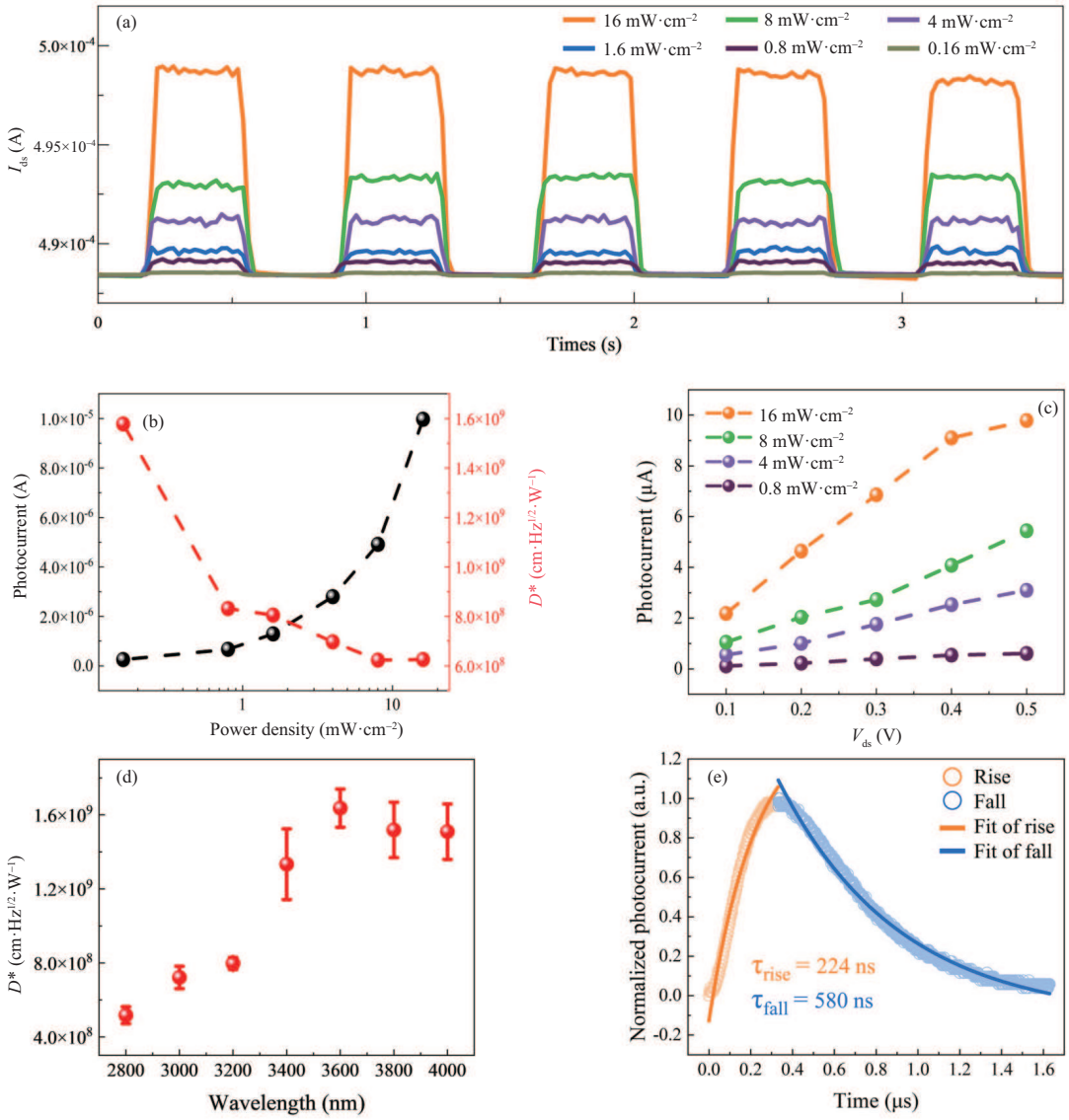

Figure 2 (Color online) Photoresponse characterization of the B-doped Si-QD/HgCdTe device. (a) Drain source current of the photodetector under different power densities at 4 μm; (b) photocurrent and specific detectivity of the photodetector as a function of the power density, V_{ds} = 0.5 V; (c) photocurrents of the photodetector as a function of V_{ds} under varying power density with a laser wavelength of 3 μm; (d) the photocurrent is a function of the wavelength, with the power density of the irradiation laser fixed at −16 mW·cm^{-2}; (e) normalized photocurrent response of the photodetector under 2.8 μm (1.5 mW), V_{ds} = 0.5 V. The solid orange (blue) curve is the fit to the original data in the orange (blue) circle.

to the change of LSPR behavior in B-doped Si QDs under a cryogenic environment. To be specific, the carrier concentration in B-doped Si QDs is decreased with lowering the temperature, which enables LSPR peak shifting to longer wavelengths. The carrier concentration dependent plasmon resonance wavelength (λ_p) can be depicted by the following equation [43–45]:

$$\lambda_p \propto 1/\omega_p = \sqrt{\frac{\varepsilon_0 m_e}{nq^2}}, \tag{5}$$

where ω_p is the bulk plasmon frequency, ε_0 is the permittivity of free space, n is the free carrier concentration, m_e is the effective mass of the free carrier, and q is the elementary charge. It should be noted that the amplitude of blackbody detectivity enhancement at 77 K is higher than that at 300 K, attributed to the increased hot-hole injection under low temperature. The detail mechanism for explaining the temperature dependent performance is illustrated in Figure 3(c). The non-radiative decay of plasmon resonance in B-doped Si QDs can cause the energy transfer from the incident photon to holes, and excites them from the valence band maximum (VBM) to higher energy levels [30, 34, 46]. The hot

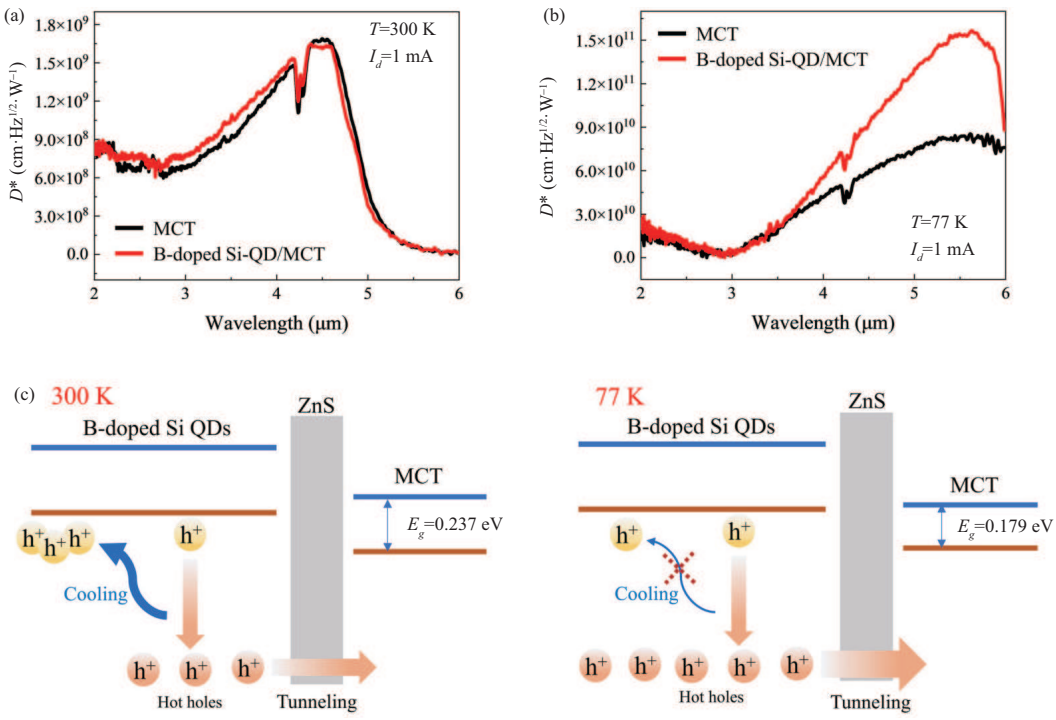

Figure 3 (Color online) (a) Blackbody detectivity of the MCT and B-doped Si-QD/MCT photodetector at different wavelengths under 300 K. (b) Blackbody detectivity of the MCT and B-doped Si-QD/MCT photodetector under 77 K. The small concavity at ∼4.25 μm in (a) and (b) is primarily due to carbon dioxide (CO_2) absorption [12]. (c) Schematic sketch of the hot-hole tunneling mechanism at different temperatures.

holes generated in B-doped Si QDs, which have sufficient kinetic energy, can tunnel directly through the ZnS barrier and inject into MCT. Under 300 K, the intra-band cooling of hot holes from high-energetic states to the edge of valence band (E_v) acts as a competition with hot-hole tunneling, which decreases the efficiency of hot-hole harvesting. While under low temperature, the cooling processes (hole-phonon scattering and phonon-phonon scattering) [47] are effectively suppressed, which dramatically increases the efficiency of hot-hole tunneling and enables higher sensitivity of the hybrid devices.

3 Conclusion

We have demonstrated an MIR photodetector with ultrafast photoresponse and outstanding sensitivity. The performance of the plasmonic B-doped Si-QD/MCT device in the MIR region is distinctly improved by the hot-hole tunneling and LSPR-enhanced light absorption. At room temperature, the device shows high specific detectivity beyond $\sim 10^9$ Jones and a fast photoresponse (∼224 ns for the rise time and ∼580 ns for the fall time). Furthermore, in a cryogenic environment, the blackbody detectivity of the Si-QD/MCT device can reach $\sim 1.6\times 10^{11}$ Jones. These results guide state-of-the-art MIR photodetector construction.

Methods. Si QDs synthesis: B-doped Si QDs were synthesized using a nonthermal plasma system whose cavity is a quartz tube [29, 30]. A mixture of three gases was used: 1:9 SiH_4/Ar mixture, 0.5:99.5 B_2H_6/Ar mixture and Ar, and their flow rates were 12, 30, and 100 sccm, respectively. The pressure in the chamber used to synthesize Si QDs was maintained at ∼3 mbar. The RF power was approximately 40 W. The 3 mg·mL^{-1} B-doped Si QDs colloids were obtained by mixing a specific ratio of B-doped Si QDs powder with absolute ethanol, followed by ultrasonication.

Si QDs characterization: The doping concentration of B-doped Si QDs was measured by inductively coupled plasma atomic emission spectrometry (ICP-AES) using a Thermal Scientific iCAP6300. To prepare TEM samples, a copper grid with ultra-thin carbon films was used as the substrate, and the colloid solution was dropped on it. Based on these prepared samples, FEI Tecnai F20 was able to conduct the TEM measurements. BRUKER IFS 66V/S was employed to do the FTIR measurements.

Photodetector fabrication: The 8 μm $Hg_{1-x}Cd_xTe$ material was grown by a mobile heating process,

where $x = 0.26$. Its shape was designed to be S-shaped, and the photosensitive surface was $\sim 6.4\times10^5$ μm^2. The upper surface of the MCT was uniformly covered with a layer of ZnS with thickness of ∼10 nm. B-doped Si QDs were spun-coated onto the MCT at 3000 r·min^{-1} and left to dry naturally.

Photoresponse measurement: The photoelectronic measurements of the photodetector were performed under the excitation of MIR laser (spot radius of ∼2 mm with tunable wavelength, Cait-T-3-4). The response time of the photodetector was measured using a pulse laser (Libra, Coherent) and OPA (OperA, Coherent). The electrical and photoresponse measurements were characterized using a Keithley 2612 analyzer at room temperature. Blackbody test data were acquired with a blackbody radiation source (HFY-200BI), a lock-in amplifier (MODEL 124A), and a current source (KEITHLEY 220 PROGRAMMABLE CURRENT SOURCE). An FTIR spectrometer (Varian 3100 FTIR Excalibur series) was used to analyze the relative spectral response. The photodetectors were placed in a dewar with a cold shield for the blackbody test (300 K and 77 K), and the temperature of the blackbody radiation source was 500 K.

Acknowledgements This work was supported by National Key Research and Development Program of China (Grant No. 2017YFA0205700), National Natural Science Foundation of China (Grant No. 61927808), Strategic Priority Research Program of Chinese Academy of Sciences (Grant No. XDB30000000), China Postdoctoral Science Foundation (Grant Nos. 2022T150121, 2021M690625), and Jiangsu Planned Projects for Postdoctoral Research Funds (Grant No. 2021K106B). The authors would like to thank Department of Infrared Devices, Shanghai Institute of Technical Physics, Chinese Academy of Sciences and Yang Wang for their help with this work.

Supporting information Appendixes A–C. The supporting information is available online at info.scichina.com and link.springer.com. The supporting materials are published as submitted, without typesetting or editing. The responsibility for scientific accuracy and content remains entirely with the authors.

References

1 Lu X W, Jiang P, Bao X H. Phonon-enhanced photothermoelectric effect in $SrTiO_3$ ultra-broadband photodetector. Nat Commun, 2019, 10: 138
2 Konstantatos G, Sargent E H. Nanostructured materials for photon detection. Nat Nanotech, 2010, 5: 391–400
3 Pan W C, Wu H D, Luo J J, et al. $Cs_2AgBiBr_6$ single-crystal X-ray detectors with a low detection limit. Nat Photonics, 2017, 11: 726–732
4 Tang X, Ackerman M M, Chen M L, et al. Dual-band infrared imaging using stacked colloidal quantum dot photodiodes. Nat Photonics, 2019, 13: 277–282
5 Wang P, Xia H, Li Q, et al. Sensing infrared photons at room temperature: from bulk materials to atomic layers. Small, 2019, 15: 1904396
6 Yu Y F, Miao F, He J, et al. Photodetecting and light-emitting devices based on two-dimensional materials. Chin Phys B, 2017, 26: 036801
7 Ge H N, Xie R Z, Guo J X, et al. Artificial micro- and nano-structure enhanced long and very long-wavelength infrared detectors. Acta Phys Sin, 2022, 71: 110703
8 An J R, Sun T, Wang B, et al. Efficient graphene in-plane homogeneous p-n-p junction based infrared photodetectors with low dark current. Sci China Inf Sci, 2021, 64: 140403
9 Liu X, Wang W H, Yang F, et al. Bi_2O_2Se/BP van der Waals heterojunction for high performance broadband photodetector. Sci China Inf Sci, 2021, 64: 140404
10 Qiu P P, Qiu W B, Lin Z L, et al. Ultra-compact tunable graphene-based plasmonic multimode interference power splitter in mid infrared frequencies. Sci China Inf Sci, 2017, 60: 082402
11 McCullough P R, Regan M, Bergeron L, et al. Quantum efficiency and quantum yield of an HgCdTe infrared sensor array. Publ Astron Soc Pac, 2008, 120: 759–776
12 Wang Y, Gu Y, Cui A L, et al. Fast uncooled mid-wavelength infrared photodetectors with heterostructures of van der Waals on epitaxial HgCdTe. Adv Mater, 2022, 34: 2107772
13 Ge H N, Xie R Z, Chen Y F, et al. Skin effect photon-trapping enhancement in infrared photodiodes. Opt Express, 2021, 29: 22823–22837
14 Camargo E G, Ueno K, Kawakami Y, et al. Miniaturized InSb photovoltaic infrared sensor operating at room temperature. Opt Eng, 2008, 47: 014402
15 Peng M, Xie R Z, Wang Z, et al. Blackbody-sensitive room-temperature infrared photodetectors based on low-dimensional tellurium grown by chemical vapor deposition. Sci Adv, 2021, 7: eabf7358
16 Zhou J, Zhou Y, Shi Y, et al. A compact polarization-integrated long wavelength infrared focal plane array based on InAs/GaSb superlattice. Sci China Inf Sci, 2022, 65: 122407
17 Rogalski A. HgCdTe infrared detector material: history, status and outlook. Rep Prog Phys, 2005, 68: 2267–2336
18 Lei W, Antoszewski J, Faraone L. Progress, challenges, and opportunities for HgCdTe infrared materials and detectors. Appl Phys Rev, 2015, 2: 041303
19 Martyniuk P, Antoszewski J, Martyniuk M, et al. New concepts in infrared photodetector designs. Appl Phys Rev, 2014, 1: 041102
20 Rogalski A, Razeghi M, Narrow gap semiconductor photodiodes. P Soc Photo-Opt Ins, 1998, 3287: 2–13
21 Meinardi F, Ehrenberg S, Dhamo L, et al. Highly efficient luminescent solar concentrators based on earth-abundant indirect-bandgap silicon quantum dots. Nat Photon, 2017, 11: 177–185
22 Linehan K, Doyle H. Size controlled synthesis of silicon nanocrystals using cationic surfactant templates. Small, 2014, 10: 584–590
23 Mastronardi M L, Maier-Flaig F, Faulkner D, et al. Size-dependent absolute quantum yields for size-separated colloidally-stable silicon nanocrystals. Nano Lett, 2012, 12: 337–342
24 Portolés M J L, Diez R P, Dell'Arciprete M L, et al. Understanding the parameters affecting the photoluminescence of silicon nanoparticles. J Phys Chem C, 2012, 116: 11315–11325

25 Hayat A, Tong J H, Chen C, et al. Multi-wavelength colloidal quantum dot lasers in distributed feedback cavities. Sci China Inf Sci, 2020, 63: 182401
26 Maier-Flaig F, Rinck J, Stephan M, et al. Multicolor silicon light-emitting diodes (SiLEDs). Nano Lett, 2013, 13: 475–480
27 Puzzo D P, Henderson E J, Helander M G, et al. Visible colloidal nanocrystal silicon light-emitting diode. Nano Lett, 2011, 11: 1585–1590
28 Rowe D J, Jeong J S, Mkhoyan K A, et al. Phosphorus-doped silicon nanocrystals exhibiting mid-infrared localized surface plasmon resonance. Nano Lett, 2013, 13: 1317–1322
29 Ni Z Y, Pi X D, Zhou S, et al. Size-dependent structures and optical absorption of boron-hyperdoped silicon nanocrystals. Adv Opt Mater, 2016, 4: 700–707
30 Ni Z Y, Ma L L, Du S C, et al. Plasmonic silicon quantum dots enabled high-sensitivity ultrabroadband photodetection of graphene-based hybrid phototransistors. ACS Nano, 2017, 11: 9854–9862
31 Chang C C, Sharma Y D, Kim Y S, et al. A surface plasmon enhanced infrared photodetector based on InAs quantum dots. Nano Lett, 2010, 10: 1704–1709
32 Zhan Q Q, Qian J, Li X, et al. A study of mesoporous silica-encapsulated gold nanorods as enhanced light scattering probes for cancer cell imaging. Nanotechnology, 2010, 21: 055704
33 Yu Y F, Sun Y, Hu Z L, et al. Fast photoelectric conversion in the near-infrared enabled by plasmon-induced hot-electron transfer. Adv Mater, 2019, 31: 1903829
34 Ng C, Cadusch J J, Dligatch S, et al. Hot carrier extraction with plasmonic broadband absorbers. ACS Nano, 2016, 10: 4704–4711
35 Pi X D, Delerue C. Tight-binding calculations of the optical response of optimally P-Doped Si nanocrystals: a model for localized surface plasmon resonance. Phys Rev Lett, 2013, 111: 177402
36 Simone G, Dyson M J, Meskers S C J, et al. Organic photodetectors and their application in large area and flexible image sensors: the role of dark current. Adv Funct Mater, 2020, 30: 1904205
37 Zhang P, Zhang Y, Wang W H, et al. Multispectral photodetectors based on 2D material/$Cs_3Bi_2I_9$ heterostructures with high detectivity. Nanotechnology, 2021, 32: 415202
38 Chen Y F, Wang Y, Wang Z, et al. Unipolar barrier photodetectors based on van der Waals heterostructures. Nat Electron, 2021, 4: 357–363
39 Chen B L, Jiang W Y, Yuan J R, et al. SWIR/MWIR InP-Based p-i-n photodiodes with InGaAs/GaAsSb Type-II quantum wells. IEEE J Quantum Electron, 2011, 47: 1244–1250
40 Zussman A, Levine B F, Kuo J M, et al. Extended long-wavelength $\lambda = 11$–15-μm GaAs/$Al_xGa_{1-x}As$ quantum-well infrared photodetectors. J Appl Phys, 1991, 70: 5101–5107
41 Hansen G L, Schmit J L, Casselman T N. Energy gap versus alloy composition and temperature in $Hg_{1-x}Cd_xTe$. J Appl Phys, 1982, 53: 7099–7101
42 Krishnamurthy S, Chen A B, Sher A, et al. Temperature dependence of band gaps in HgCdTe and other semiconductors. J Electron Mater, 1995, 24: 1121–1125
43 Garcia G, Buonsanti R, Runnerstrom E L, et al. Dynamically modulating the surface plasmon resonance of doped semiconductor nanocrystals. Nano Lett, 2011, 11: 4415–4420
44 Agrawal A, Kriegel I, Milliron D J. Shape-dependent field enhancement and plasmon resonance of oxide nanocrystals. J Phys Chem C, 2015, 119: 6227–6238
45 Kasani S, Zheng P, Bright J, et al. Tunable visible-light surface plasmon resonance of molybdenum oxide thin films fabricated by E-beam evaporation. ACS Appl Electron Mater, 2019, 1: 2389–2395
46 Mubeen S, Hernandez-Sosa G, Moses D, et al. Plasmonic photosensitization of a wide band gap semiconductor: converting plasmons to charge carriers. Nano Lett, 2011, 11: 5548–5552
47 Chuang C H, Chen X B, Burda C. Femtosecond time-resolved hot carrier energy distributions of photoexcited semiconductor quantum dots. Annalen Der Physik, 2013, 525: 43–48